In situ observations of velocity changes in response to tidal deformation from analysis of the high-frequency ambient wavefield

G. Hillers, L. Retailleau, M. Campillo, A. Inbal, J. -P. Ampuero, T. Nishimura

▶ **To cite this version:**

G. Hillers, L. Retailleau, M. Campillo, A. Inbal, J. -P. Ampuero, et al.. In situ observations of velocity changes in response to tidal deformation from analysis of the high-frequency ambient wavefield. Journal of Geophysical Research : Solid Earth, 2015, 120, pp.210-225. 10.1002/2014JB011318 . insu-03580034

HAL Id: insu-03580034

https://insu.hal.science/insu-03580034

Submitted on 18 Feb 2022

HAL is a multi-disciplinary open access archive for the deposit and dissemination of scientific research documents, whether they are published or not. The documents may come from teaching and research institutions in France or abroad, or from public or private research centers.

L'archive ouverte pluridisciplinaire **HAL**, est destinée au dépôt et à la diffusion de documents scientifiques de niveau recherche, publiés ou non, émanant des établissements d'enseignement et de recherche français ou étrangers, des laboratoires publics ou privés.

Copyright

AGU PUBLICATIONS

JGR

Journal of Geophysical Research: Solid Earth

RESEARCH ARTICLE

10.1002/2014JB011318

Key Points:
- Analysis of the ambient wavefield resolves tidal-induced velocity changes
- Shallow wave speeds are reduced during periods of volumetric compression
- The response indicates nonlinear elasticity of the dilatant shallow material

Correspondence to:
G. Hillers,
gregor.hillers@ujf-grenoble.fr

Citation:
Hillers, G., L. Retailleau, M. Campillo, A. Inbal, J.-P. Ampuero, and T. Nishimura (2015), In situ observations of velocity changes in response to tidal deformation from analysis of the high-frequency ambient wavefield, *J. Geophys. Res. Solid Earth*, *120*, 210–225, doi:10.1002/2014JB011318.

Received 23 MAY 2014
Accepted 26 NOV 2014
Accepted article online 5 DEC 2014
Published online 7 JAN 2015

In situ observations of velocity changes in response to tidal deformation from analysis of the high-frequency ambient wavefield

G. Hillers[1], L. Retailleau[2], M. Campillo[1], A. Inbal[3], J.-P. Ampuero[3], and T. Nishimura[4]

[1]Institut des Sciences de la Terre, Joseph Fourier University, CNRS, Grenoble, France, [2]Institut de Physique du Globe de Paris, Sorbonne Paris Cité, CNRS, Paris, France, [3]Seismological Laboratory, California Institute of Technology, Pasadena, California, USA, [4]Department of Geophysics, Tohoku University, Sendai, Japan

Abstract We report systematic seismic velocity variations in response to tidal deformation. Measurements are made on correlation functions of the ambient seismic wavefield at 2–8 Hz recorded by a dense array at the site of the Piñon Flat Observatory, Southern California. The key observation is the dependence of the response on the component of wave motion and coda lapse time τ. Measurements on the vertical correlation component indicate reduced wave speeds during periods of volumetric compression, whereas data from horizontal components show the opposite behavior, compatible with previous observations. These effects are amplified by the directional sensitivities of the different surface wave types constituting the early coda of vertical and horizontal correlation components to the anisotropic behavior of the compliant layer. The decrease of the velocity (volumetric) strain sensitivity S_θ with τ indicates that this response is constrained to shallow depths. The observed velocity dependence on strain implies nonlinear behavior, but conclusions regarding elasticity are more ambiguous. The anisotropic response is possibly associated with inelastic dilatancy of the unconsolidated, low-velocity material above the granitic basement. However, equal polarity of vertical component velocity changes and deformation in the vertical direction indicate that a nonlinear Poisson effect is similarly compatible with the observed response pattern. Peak relative velocity changes at small τ are 0.03%, which translates into an absolute velocity strain sensitivity of $S_\theta \approx 5 \times 10^3$ and a stress sensitivity of 0.5 MPa^{-1}. The potentially evolving velocity strain sensitivity of crustal and fault zone materials can be studied with the method introduced here.

1. Introduction

Analyzing the response to perturbations is a fundamental scientific method to study properties of a target system. In modern rock mechanics, this concept has been applied to investigate the behavior of geomaterials under controlled laboratory conditions in response to a variety of stimuli [e.g., *Ostrovsky and Johnson*, 2001; *Scholz*, 2002; *Jaeger et al.*, 2007]. Testing strategies range from (quasi-) static over cyclic to dynamic stress histories or deformation protocols [e.g., *Lockner et al.*, 1977; *Holcomb*, 1981; *Pasqualini et al.*, 2007] and include acoustic [e.g., *Johnson et al.*, 2008] and resonant excitation [e.g., *Renaud et al.*, 2012], applied under a wide range of confining stress conditions. This can induce linear and nonlinear elastic or nonelastic behavior, where the response type is critically governed by the distribution and properties of voids or (micro-) cracks within the probed material, i.e., by its damage state [e.g., *Lyakhovsky et al.*, 1997; *Hamiel et al.*, 2006]. Observations constrain theoretical frameworks targeting the description of multiscale rheology including the linear elastic responses exhibited by competent rock to infinitesimal strains, the asymmetric responses for loading under compression and tension of damaged solids, and the dynamics of granular materials excited by dynamic stimuli [e.g., *Ben-Zion*, 2008, and references therein]. However, the scale dependence poses a fundamental problem in formulating constitutive relationships, because sample size and the associated distribution of defects control the macroscopic rheology of composite Earth materials [*Scholz*, 2002; *Jaeger et al.*, 2007]. Hence, in situ observations covering a large range of spatiotemporal scales are keys for a universal assessment of rock behavior.

Under natural or in situ conditions, crustal rocks—particularly those situated in lithospheric boundary regions along zones of localized deformation—are also deformed by a variety of loading mechanisms that originate within solid Earth and the atmosphere. Deformation patterns can be associated with tectonic loading, slow or rapid slip on earthquake faults, fluid migration, variable water content in sedimentary

©2014. American Geophysical Union. All Rights Reserved.

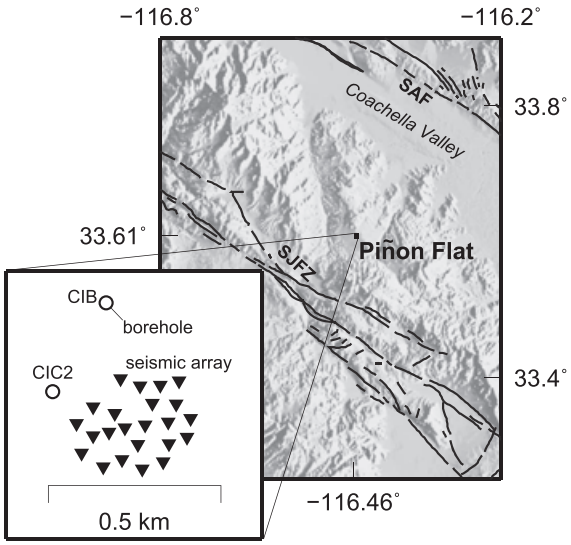

Figure 1. Shaded relief map of the study area. The Piñon Flat Observatory (PFO) is located on a granitic plateau at ~1300 m elevation in the San Jacinto Mountains. High-frequency noise is generated in the Coachella Valley north northeast to the site. The inset illustrates the array geometry and the location of two boreholes. Topography at the site controls that seismic stations to the northeast are located about 15 m higher compared to southwest stations. Black lines show geologically mapped faults. SJFZ: San Jacinto Fault Zone. SAF: San Andreas Fault.

basins, barometric pressure changes, thermoelastic strains, and tides. Resolving the sensitivity of different crustal materials to a range of continuous, periodic, or transient strains with variable duration and amplitude is expected to improve the understanding of earthquake nucleation and to explain variations in seismicity patterns.

The relation between elastic moduli and wave speed allows the probing of rock properties by monitoring seismic velocity changes [e.g., *Lockner et al.*, 1977]. Measuring in situ responses to Earth tides is an appealing strategy because of the evident tidal effect on crustal deformation [*Tsuruoka et al.*, 1995; *Custodio et al.*, 2003; *Stroup et al.*, 2007; *Nakata et al.*, 2008; *Rubinstein et al.*, 2008] associated with the relatively well understood stress history. Routine velocity monitoring is, however, complicated by the dependence on a repetitive, controlled source such as industrial machinery [*Reasenberg and Aki*, 1974], vibrators, air guns, and piezoelectric transducers [*Yamamura et al.*, 2003, and references therein].

Alternatively, the analysis of Green's function estimates constructed from the ambient seismic wavefield has become a standard tool for velocity change monitoring [e.g., *Campillo et al.*, 2011, and references therein]. Techniques targeting the multiple-scattered coda wavefield of interstation noise correlation functions provide the opportunity to measure velocity changes over times and distances that are governed by the properties of the coherent parts of the noise wavefield. In this article, we present an approach to measure relative velocity variations (dv/v) in response to tidal deformation by analyzing noise recorded by a dense seismic array.

The key observation is the resolution of a systematic dependence of the dv/v amplitude on travel time or lapse time, on the deformation direction and on the component of the empirical Green's tensor, i.e., on the wavefield component. These observations indicate that the in situ strain sensitivity of the unconsolidated material at the observation site is depth dependent and anisotropic. In the first part of our presentation (section 2) we explain technical aspects of the method focusing on the assessment of the robustness of the results. After presenting the observations (section 3), we conclude with a discussion of a variety of mechanisms (section 4) that potentially govern the observed response, which is in contrast to previous in situ observations [e.g., *Reasenberg and Aki*, 1974; *Bungum et al.*, 1977]. The resolution of peak relative changes $dv/v = 0.03\%$ in response to tidal volumetric strain on the order of 25 nanostrain demonstrated here suggests a potentially widespread application of the method for the systematic investigation of in situ responses.

2. Data and Method

2.1. Seismic Data and Site Conditions

A temporary seismic array was installed at the site of the Piñon Flat Geophysical Observatory (PFO) (Figure 1). The array consists of 26 short-period three-component (N, E, and Z) sensors with an interstation distance of ~50 m and is characterized by an approximately circular geometry with a diameter of ~400 m. It is located next to two boreholes where the groundwater table is monitored. We use data from 23 stations collected between day 70 and 220 in 2011.

©2014. American Geophysical Union. All Rights Reserved.

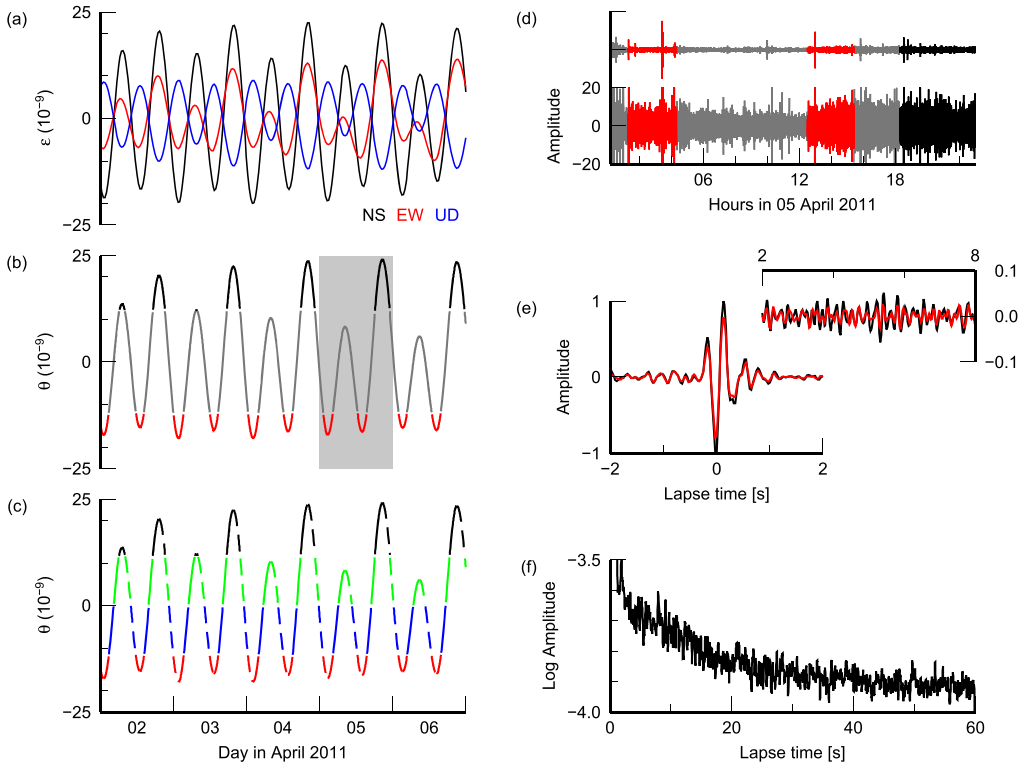

Figure 2. Illustration of the analysis. (a) Tidal strains at PFO in the north-south, east-west, and up-down directions. (b) Volumetric deformation protocol and determination of time windows associated with the threshold method. Positive and negative values correspond to extension and compression, respectively. (c) The segment method defines time windows based on strain amplitude and rate. (d) Vertical component seismograms from two stations recorded on 5 April 2011 (gray area in Figure 2b). Black and red segments correspond to the extension and compression periods indicated in Figure 2b. Data are band pass filtered between 2 and 8 Hz. Amplitudes in both traces are on the same scale. (e) Correlation functions associated with different deformation periods stacked over 90 days. The small interstation distance yields a main arrival around $\tau = 0$ s. Relative arrival time changes are measured in the coda at $|\tau| > 1$ s. Positive dv/v values in Figure 3 are associated with delayed arrivals in the red waveforms compared to phases in the black coda. (f) The logarithm of the average noise correlation coda envelope is used to determine the lapse time analysis range.

PFO is located some 20 km northeast of the San Jacinto Fault on the Southern California Peninsular Ranges batholith at an altitude of ~1300 m. The local geology is characterized by a ~1 m thick surface layer of almost totally decomposed granodiorite which grades into grus and corestones and then into intact granite at an average depth of ~25 m [*Wyatt*, 1982]. The thickness of the transitional layer varies significantly, and its subsurface topography exhibits a complex 3-D structure. The associated velocity profiles are thus characterized by a steep gradient. In contrast to the wave speeds in the soil layer which are not much different from the speed of sound in air [*Vernon et al.*, 1998], *P* wave velocities in the basement below ~60 m depth reach almost 5.5 km/s [*Fletcher et al.*, 1990; *Hong and Menke*, 2006; *Allam and Ben-Zion*, 2012]. The combined heterogeneity and low velocities in the top 25 m cause high attenuation, strong scattering, and reverberation effects in the near-surface waveguide [*Fletcher et al.*, 1990; *Vernon et al.*, 1998; *Wagner*, 1998].

2.2. Tides

Tides at PFO are predicted based on harmonic constants obtained with the long-baseline laser strainmeter that is part of the instrumentation at the observatory (D. Agnew, personal communication, 2013; e-mail from 8 March 2013). That is, we focus on clean tidal deformation time series and neglect observed strain components associated with tectonic loading and transients [*Agnew and Wyatt*, 2014]. We chose this approach to simplify the analysis. However, as demonstrated below, nontidal strain may interfere with the tides over the duration of the analysis period.

We start with two time series of strain in north-south ($\varepsilon_{NS} = \varepsilon_{yy}$) and east-west ($\varepsilon_{EW} = \varepsilon_{xx}$) directions that cover the time period of seismic data availability (Figure 2a). From this, we compute areal $\varepsilon_{xx} + \varepsilon_{yy}$ and

©2014. American Geophysical Union. All Rights Reserved.

volumetric strain $\theta = \varepsilon_{xx}+\varepsilon_{yy}+\varepsilon_{zz}$. Vertical strain $\varepsilon_{UD} = \varepsilon_{zz}$ is related to areal strain through $\varepsilon_{zz} = \zeta(\varepsilon_{xx}+\varepsilon_{yy})$, where $\zeta = -\nu/(1-\nu) = -1/3$ and $\nu = 1/4$ is Poisson's ratio. The negative ζ indicates that during episodes of areal, i.e., horizontal, tidal compression the crust is extended in the vertical direction and vice versa. The relation between vertical and areal strain holds at the surface of a traction-free half-space. It is sufficiently accurate for the purpose of our analysis [*DeWolf*, 2014].

We apply two strategies to define time segments associated with specific characteristics of the volumetric strain history. First, for the *threshold method* (Figure 2b), segments are defined by times during which θ is smaller and larger than a negative and positive strain limit, respectively. Second, for the *segment method* we choose three limits (Figure 2c), one at $\theta = 0$ and two limits at negative and positive θ that half the range of absolute θ values. We further distinguish segments with increasing or decreasing θ. This leads to eight segments controlled by strain amplitude and rate.

2.3. Correlations

Seismic data are preprocessed following *Poli et al.* [2012] to mitigate the effects of earthquakes and transients and to optimize the signal-to-noise ratio (SNR) of noise correlations. Algorithmic tuning parameters for the removal of large-amplitude episodes are adopted from a noise tomography study in the Southern California plate boundary region [*Zigone et al.*, 2014]. Correlations are scaled by an estimate of the total power in the seismograms (Figure 2e), which yields estimates of the coherency C confined between −1 and 1. C functions are obtained by correlating data from segments with a minimum duration of 30 min. The 0–2 correlations per day associated with a specific deformation state are then stacked over d days using weights proportional to the square root of the time window duration [*Sabra et al.*, 2005; *Larose et al.*, 2007]. For each station and component of ground motion, this yields two $C_{1,2}$ functions associated with positive and negative strain for the threshold method and eight corresponding $C_{1,\ldots,8}$ functions for the segment method.

2.4. Velocity Change Estimates

In situ active source methods analyze velocity changes using variations in the travel time τ of ballistic phases between source and receiver [*Reasenberg and Aki*, 1974; *Yamamura et al.*, 2003; *Silver et al.*, 2007; *Niu et al.*, 2008]. The resolution of relative travel time changes $d\tau/\tau$ can be tuned by optimizing the experimental parameters [*Silver et al.*, 2007]. In contrast, the precision of travel time changes of direct arrivals extracted from C functions is limited in practice [*Weaver et al.*, 2009] because the required stationarity and isotropy of the ambient wavefield is only approximately met. For this reason $d\tau/\tau$ estimates are extracted from scattered arrivals in the coda of the correlation functions (Figure 2e), where the phase delay accumulates linearly for homogeneous medium changes. The approach, which was first applied to earthquake coda [*Poupinet et al.*, 1984], increases the sensitivity of noise seismology tools because scattered correlation coda waves are less sensitive to fluctuations in the excitation mechanism.

We apply a time domain technique (stretching) [*Lobkis and Weaver*, 2003; *Wegler and Sens-Schönfelder*, 2007] and a frequency domain technique (doublet) [*Poupinet et al.*, 1984; *Brenguier et al.*, 2008] to estimate relative velocity changes $dv/v = -d\tau/\tau$. Both approaches compare a test waveform to a reference waveform. In seismological monitoring contexts [*Sens-Schönfelder and Wegler*, 2006; *Brenguier et al.*, 2008] test waveforms are usually consecutive correlations made from one to tens of days of data, and the reference waveform is a correlation or stack consisting of all data from an observation period. In the present case, two functions C_i, C_j associated with a state of tidal deformation are compared.

For the stretching technique, the waveform under investigation is dilated (compressed or stretched) to find the best similarity (highest correlation coefficient) with the reference waveform. The optimal coefficient of dilation is an estimate of the velocity change. Estimating dv/v with the doublet or moving window cross-spectral technique [*Clarke et al.*, 2011] consists of two regressions. First, the delay time $d\tau$ is estimated from the cross-spectral phase shift along the frequencies of interest for multiple time windows centered at consecutive times τ. Second, the trend of resulting $d\tau$ estimates as a function of τ yields the relative change $d\tau/\tau$. The longest period in the frequency band controls the size of these moving windows, i.e., several of them are contained in each window of the lapse time analysis discussed below.

A comparison of the results obtained with the two techniques is indicative of the robustness of an estimate, because they perform different in the presence of fluctuations [*Hadziioannou et al.*, 2009; *Zhan et al.*, 2013].

©2014. American Geophysical Union. All Rights Reserved.

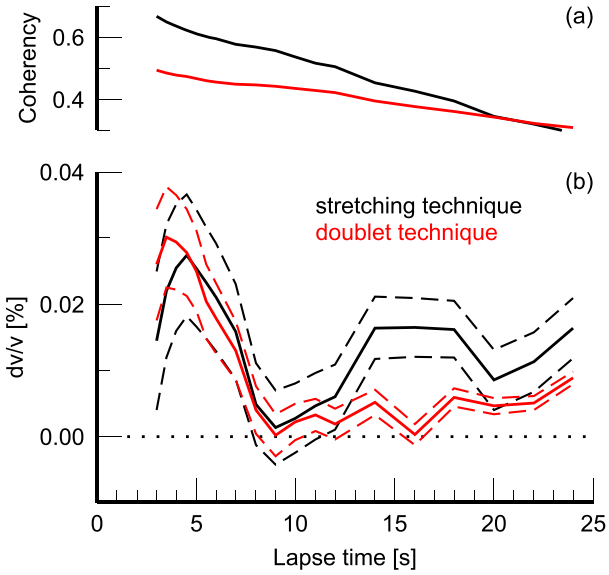

Figure 3. (a) Average coherency estimates as a function of lapse time. For the stretching technique, this measure refers to the correlation coefficient associated with optimal dilation of the waveform. For the doublet technique, it indicates the coherency between the windowed waveforms and is therefore consistently lower. (b) Relative velocity change as a function of lapse time obtained with the threshold method. Overall, the uncertainty of the doublet technique estimates is reduced due to the weighted inversion. We used data from 23 stations and 80 days stacks of 2–8 Hz ZZ correlations. Errors are computed using the estimates of *Weaver et al.* [2011] and *Clarke et al.* [2011] for the stretching and doublet technique, respectively.

Measurements between two individual C_i, C_j lead to one and 28 independent dv/v estimates for the threshold and segment method, respectively. We consider ZZ, NN, and EE correlations, which represent the medium response parallel to the direction of the (virtual) excitation.

For each component (ZZ, NN, and EE) and segment (*ij*) pair, the dv/v estimates obtained with the stretching technique are averaged over the 253 station pairs, a number that is reduced in practice due to data acquisition and quality problems. Meaningful dv/v values obtained with the stretching technique exceed the root-mean-square (RMS) of an apparent waveform dilation that depends nonlinearly on signal coherency, frequency, bandwidth, and duration [*Weaver et al.*, 2011]. Weights associated with the two regressions constituting the doublet technique [*Clarke et al.*, 2011] allow a simultaneous inversion of all data [*Zaccarelli et al.*, 2011], which leads to uncertainties that are typically smaller compared to the stretching technique.

The analyses are performed in different frequency bands using band pass-filtered versions of the original broadband correlation functions (whitening is applied in a 4 s–20 Hz range). Here we focus on the 2–8 Hz range, and we measure relative velocity changes in 4 s long lapse time windows beginning at $|\tau| = 1$ s. We find that the ratio of 8 between window length and smallest period reduces the uncertainties to an acceptable level [*Weaver et al.*, 2011; *Clarke et al.*, 2011] for this data set and application. An estimate of the meaningful upper τ limit can be obtained from the decay behavior of the average coda envelope (Figure 2f). Arrivals with energy above an asymptotic background level that can be estimated at very late lapse times (here between 40 s and 60 s) are associated with strong multiple-scattered phases, in contrast to the incoherent noise that dominates waveforms in the tail. Note, however, that coherent energy still arrives after the transition limit, which facilitates the reconstruction of the Green's function by recorrelating correlation coda [*Stehly et al.*, 2008]. We find that the transition occurs between 25 s and 30 s; hence, we limit the lapse time-dependent analysis to 26 s. To maintain good resolution at short lapse times where the response changes fast the windows overlap 3.5 s to $\tau = 6$ s (4–8 s), then 3 s to $\tau = 12$ s, and finally 2 s to $\tau = 24$ s.

3. Results

3.1. Threshold Method

The key observation obtained with the threshold method from ZZ correlations is shown in Figure 3. We resolve relative velocity changes of ~0.03% in the first few seconds and an overall decay of dv/v with increasing lapse time. The consistency of the results obtained with the stretching and the doublet technique imply a high fidelity of these observations. Significant discrepancies appear at $\tau > 12$ s. The average differential strain $d\theta$ between volumetric compression and extension periods above and below the ±13 nanostrain threshold (Figure 2a) is 36 ± 5 nanostrain. We can thus estimate a velocity (volumetric) strain sensitivity $S_\theta = dv(v\,d\theta)^{-1} = (10 \pm 2) \times 10^3$. Note that positive dv/v amplitudes are associated with a reduction of wave speeds during volumetric compression episodes. We address this strain dependence in section 4. Performing these measurements in various frequency bands, we find that high-frequency

©2014. American Geophysical Union. All Rights Reserved.

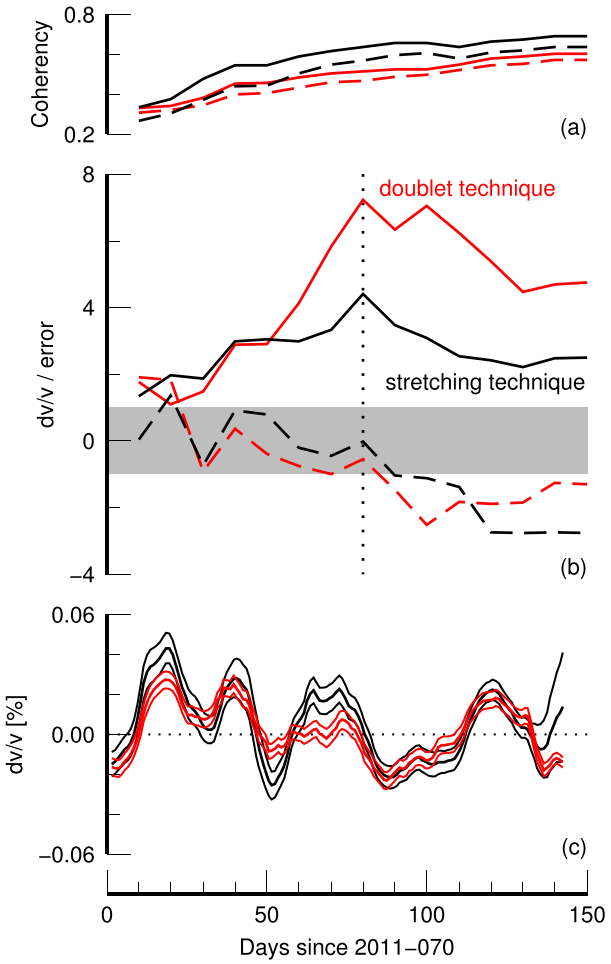

Figure 4. (a, b) Dependence of the velocity change resolution on time and (c) the long-term dv/v evolution. In Figure 4b we show the evolution of dv/v estimates scaled by the corresponding uncertainties. Absolute values larger than unity above or below the gray area indicate well-resolved measurements. Results are obtained from 2–8 Hz ZZ correlations using the threshold method. In Figures 4a and 4b the solid (dashed) lines correspond to a lapse time window centered on 4 s (9 s). The vertical line at 80 days in Figure 4b corresponds to results in Figure 3b. Figure 4c shows the corresponding long-term dv/v evolution (estimated using standard procedure [e.g., *Hillers et al.*, 2014]) obtained with the stretching and the doublet technique (2–8 Hz frequency range, τ = 2–8 s, ZZ component). At each datum, correlations from ±7 days are stacked, and the resulting time series is smoothed with a 11 day running average.

large-bandwidth analyses yield best results in terms of time domain and frequency domain consistency, and we therefore focus in our analysis on the 2–8 Hz range. Similar yet less consistent signals obtained with lower and higher central frequencies indicate that our results are not biased by intermittent transients characterized by a 3–4 Hz spectral peak associated with traffic in the Coachella Valley.

3.1.1. Temporal Averaging

We explore the resolution as a function of temporal averaging by repeating the measurements for successively increasing time periods (d = 10–150 days in 10 day increments; the beginning of the time period is fixed) using data from all stations. We analyze the emerging dv/v signal scaled by the associated uncertainties. Figure 4 indicates the buildup of a relatively robust signal at small τ after about 10–20 days and the SNR peaks around 80 days. In general, results from the doublet technique are characterized by larger SNR, due to the weighted fitting procedure. However, error reduction associated with the buildup in coherency (Figure 4a) does not translate into the expected continuous increase of the signal strength (Figure 4b).

We attribute this to the interference of the tidal velocity change with dv/v responses to various external or internal forcing mechanisms (Figure 4c). Potential driving mechanisms include changes in the atmospheric pressure and temperature field [*Gao et al.*, 2000; *Richter et al.*, 2014], variations in the groundwater table [*Sens-Schönfelder and Wegler*, 2006], or strain transients in the study area [*Agnew and Wyatt*, 2014]. These long-term velocity variations are usually of greater amplitude compared to the tidal response. The simultaneity of the tidal peak SNR (Figure 4b) and the long-term dv/v polarity change around 80 days (Figure 4c) supports the assumed interference: The change of the ambient state blurs or masks the tidal component with increasing stack time. The situation is reversed for later lapse times (dashed lines in Figures 4a and 4b), where a weak opposite strain sensitivity emerges with increasing averaging time. It illustrates the trade-offs associated with the choice of the averaging window, which has to balance competing effects of coherency buildup and ambient dv/v variations.

3.1.2. Network Size

The resolution of the observed signal benefits from averaging over a large number of station pairs. Figure 5 demonstrates the dependence of the signal strength as a function of network size averaging over 90 days.

©2014. American Geophysical Union. All Rights Reserved.

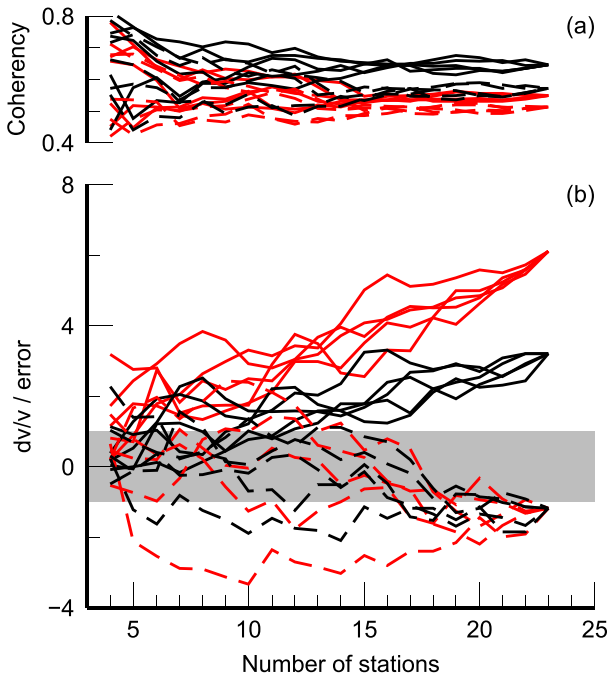

Figure 5. Dependence of the velocity change resolution on the number of stations. (a, b) Individual lines correspond to five different random choices in assembling the growing network. The values in Figure 5b at 23 stations correspond to values in Figure 4b at 90 days.

For this test we repeat the measurements by increasing the virtual network size from 4 to 23 stations using five different random walks across the array. This analysis confirms the superior performance of the doublet method, indicating that averaging over as few as five stations is sufficient to resolve the velocity change at small τ. In contrast, the stretching method needs 10–15 stations to resolve a dv/v estimate. The behavior at later lapse times is characterized by a strong dependence of the SNR on the random path, particularly for the results of the doublet method. This weakens the reliability of the associated late τ signals in Figure 4b.

3.2. Segment Method

For the segment method (Figure 2c) we use the doublet technique only because we find that the associated uncertainties are consistently smaller compared to the stretching approach. We discuss results from an averaging time window of 60 days after testing windows of 30, 60, 90, and 120 days duration. For the lapse time-dependent analysis, we use the same 4 s windows as in the threshold method, because shorter coda windows lead to significantly increased uncertainties. We extend the ZZ correlation analysis to the NN and EE pairs.

The segment method has the advantage of potentially improving the resolution if threshold method results are at or below the resolution limit, which balances the disadvantage of being computationally more expensive. The increased processing costs are attributed to the larger number of dv/v analyses between possible ij pairs. The associated estimates populate a $d\theta$–dv/v plane (Figure 6), where $d\theta$ denotes again the average differential volumetric strain between analyzed segments ij. For each lapse time, the strain sensitivity S_θ (Figure 7) is inferred from the slope of a linear regression of dv/v as a function of $d\theta$. Because dv/v and $d\theta$ errors are very similar for each datum, we do not apply weights in the least squares fit.

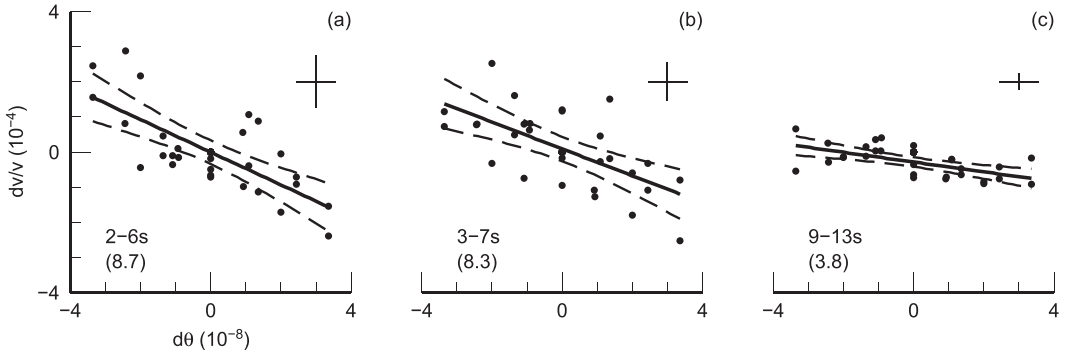

Figure 6. Results of the segment method at different lapse time windows (ZZ component; 2–8 Hz; doublet technique). Each datum represents the relative dv/v measurement associated with one θ segment pair (Figure 2c). The slope indicates the velocity sensitivity to volumetric strain changes, $d\theta$. Negative trends are associated with reduced wave speeds during volumetric and areal compression and vertical extension. The crosses denote the typical uncertainty of each datum. The value in parenthesis is the root-mean-square error (scaled to 10^{-5}) of the linear fit. Smaller values imply better fits associated with less scatter.

©2014. American Geophysical Union. All Rights Reserved.

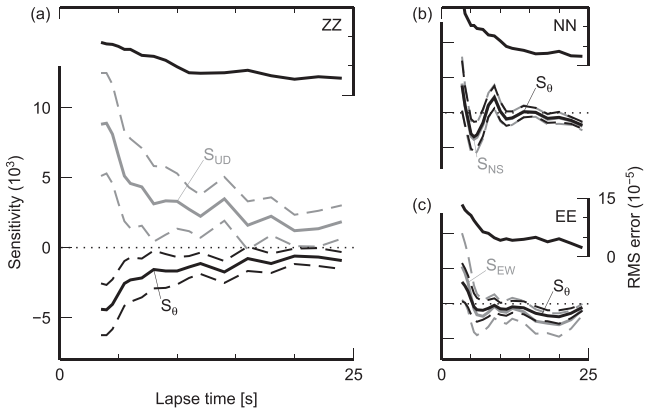

Figure 7. Velocity sensitivity S as a function of lapse time for (a) ZZ, (b) NN, and (c) EE correlations. Each datum corresponds to the slope of a fitted line illustrated in Figure 6. Black data indicate sensitivity to volumetric deformation. Gray data indicate the response to the component of deformation that is parallel to the force direction and receiver component. The RMS errors indicate significant scatter at small lapse times on the horizontal components. All graphs are on the same scale.

Alternatively, we obtain the sensitivities S_{UD}, S_{NS}, and S_{EW} from the ε_{UD}, ε_{NS}, and ε_{EW} time series (Figure 2a), which allows estimates of the response to the component of deformation that is parallel to the couple consisting of the virtual source direction and excited component of wave motion. For this, we calculate new fits using $d\varepsilon$ data associated with each of the three directions (gray data in Figure 7), but the segmentation information is obviously taken from the original θ time series. With $\zeta = -1/3$, $\varepsilon_{NS} \approx \theta$ (Figures 2a and 2b) at PFO, and hence, $\varepsilon_{UD} \approx -\theta/2$ and $\varepsilon_{EW} \approx \theta/2$.

In principle, analysis of the differential response between individual segments can resolve potential hysteresis effects that indicate inelastic rheology. That is, the observed scatter around the mean trend at early lapse times, which is most significant in NN and EE data, can possibly be associated with an asymmetric response under loading and unloading. Here we consider uncertainties associated with individual *ij* measurements too significant to resolve a meaningful hysteresis loop. The application of correlation denoising techniques [*Stehly et al.*, 2011] can reduce the uncertainties of dv/v estimates, therefore allowing estimates of dissipation from the area enclosed by a hysteresis loop. Note that the observed origin interception (Figure 6) is not forced in the parametrization.

The lapse time dependence estimated from ZZ correlations with the segment method is generally consistent with observations from the threshold method (Figures 7a and 3b). The magnitude of the peak sensitivity S_θ at early lapse times of $(4.4 \pm 1.3) \times 10^3$ is about half of the $(10 \pm 2) \times 10^3$ estimate obtained with the threshold method. Differences appear at times τ around and greater 10 s. We have greater confidence in the segment method results considering the more reliable dv/v-$d\theta$ regressions (Figure 6c) compared to the threshold estimates based on a single differential measurement. These numbers further indicate that the uncertainty using the segment method is reduced by ~30%.

The horizontal NN and EE response to volumetric deformation exhibits a more complex τ dependence compared to the vertical data. In particular, both estimates show a positive sensitivity at small τ, which is associated with faster wave speeds during volumetric and areal compression. The responses indicate that component averaging with the intention to increase the SNR [*Schaff*, 2012] is a bad strategy in the present case.

4. Discussion

In this section we discuss the validity (section 4.1) and depth range (section 4.2) of the complex response pattern. We then evaluate a range of physical mechanisms that are ultimately driven by tidal deformation for their potential influence on the observed velocity changes. Although the groundwater table changes systematically with the tides, we demonstrate that our observations are not compatible with water level-driven dv/v variations (section 4.3). We argue that dilatant effects can play an important role in explaining the vertical component results that are opposite to previous observations (section 4.4). Finally, we consider the decomposition of the volumetric sensitivity S_θ into orthogonal components (section 4.5).

4.1. Diurnal Variations

We find that our results are not biased by obvious changes of wavefield properties, i.e., diurnal amplitude changes. Similar to *Hillers et al.* [2014], seismic wave speed monitoring at PFO at frequencies above 1 Hz rests on the analysis of noise that has a strong cultural component in addition to natural high-frequency sources such as wind [*Hillers and Ben-Zion*, 2011]. Wind farms, agricultural activity, and transportation in

©2014. American Geophysical Union. All Rights Reserved.

the Coachella Valley (Figure 1) constitute perhaps the strongest sources of high-frequency noise excitation. *Hillers et al.* [2012] discussed that in addition to noise amplitude, the wavefield coherency can similarly be affected by a systematic variation in the excitation mechanism, potentially introducing a bias. We tested this by performing dv/v measurements on correlation functions that were constructed from diurnal data. That is, we replaced segmentation based on the tides with daytime and nighttime segmentation and stacked data from tens of days and nights. This analysis did not return a more consistent or higher dv/v signal that could imply a spurious measurement caused by a systematic noise excitation pattern. It also rules out a governing effect of diurnal temperature changes, although an effect of temperature on the shallow velocity structure cannot be excluded [*Richter et al.*, 2014].

4.2. Depth Sensitivity

Lapse time variations of dv/v are related to systematic changes in the depth sensitivity of correlation coda waves as a function of τ [*Obermann et al.*, 2013]. Waves that propagated near the surface constitute early arrivals. Governed by scattering and wave conversions, the probability that an arrival has sampled deeper parts increases with τ. The rate at which this sensitivity change occurs depends on the heterogeneity of the medium. For the ZZ component, *Obermann et al.* [2013] showed that the partitioning between surface and body wave sensitivity balances at a lapse time of about 6 times the scattering mean free time t^*, which is a measure of the average time between two scattering events.

The extend to which these conclusions can be applied to the situation at PFO is debatable. *Obermann et al.* [2013] conducted numerical experiments for a scattering 2-D medium where fluctuations are superimposed on a constant background velocity. However, the degraded, low-velocity upper layer at PFO has been demonstrated to act as a waveguide for refracted and scattered high-frequency waves [*Vernon et al.*, 1998; *Wagner*, 1998]. Shear wave velocities are smaller than 200 m/s at the surface and increase to 900–1600 m/s at 10–20 m depth, so waves recorded on the horizontal components at higher frequencies in the 2–8 Hz band are likely guided and predominantly scattered in horizontal directions, which would increase the factor of 6.

Rayleigh waves dominate single-scattered waves after the main arrival at small τ on the ZZ component [*Margerin et al.*, 2009]. We estimate the surface wave depth sensitivity [e.g., *Herrmann*, 2006] for the vertical velocity profile from *Fletcher et al.* [1990] and find that the eigenfunctions of 2 Hz (8 Hz) Rayleigh waves peak in the top 30 m (10 m). The strong heterogeneity and complex subsurface geology imply a relatively short mean free time, which is supported by observations of substantially distorted wavefields on scale lengths of the order of the seismic array [*Vernon et al.*, 1991]. Indeed, studying equipartition properties using 5–7 Hz earthquake coda waveforms recorded at PFO, *Margerin et al.* [2009] conclude that t^* "is very small, of the order of a few seconds only." This is compatible with the 1–10 km estimate of the scattering mean free path from 7 Hz earthquake coda phase statistics [*Anache-Ménier et al.*, 2009]. We thus attribute the overall decreasing sensitivities with τ (Figure 7a) to characteristics of a depth-dependent response and relate the strongest velocity changes to the weathered material overlying the granitic basement.

The observed lapse time dependence of the velocity variations is comparable to thermally driven near-surface velocity changes on the Moon [*Obermann et al.*, 2013, Figure 14]. Similar to the present situation, the interstation distance of the lunar array was around 60 m, and the analyzed frequency band overlaps with the one in our analysis [*Larose et al.*, 2005]. Moreover, the ZZ signal shape from both sites is very similar, i.e., it exhibits a peak at ~3 s which is followed by a decay toward 10 s to the tail level. We conclude that the responses at PFO and at the site of the Apollo 17 Lunar Seismic Profiling Experiment are considerably similar. It suggests comparable rock properties of unconsolidated materials close to the surface of the respective celestial body.

Our observation of reduced seismic wave speeds at all lapse times in the ZZ component and at late lapse times in the NN and EE components during volumetric tidal compression episodes is contradictory to previous observations of near-surface velocity variations ($O(10^{-3})$) in response to tidal loads [*Reasenberg and Aki*, 1974; *Bungum et al.*, 1977; *Yamamura et al.*, 2003; *Takano et al.*, 2014]. The obtained dv/v values are an order of magnitude larger compared to our $O(10^{-4})$ estimates. The governing mechanism was identified as tensile opening and closing of cracks—also referred to as "clapping"—at very shallow depths [*Reasenberg and Aki*, 1974]. In the following we discuss potential mechanisms that can control the observed opposite behavior, focusing on the large ZZ signal at small τ.

©2014. American Geophysical Union. All Rights Reserved.

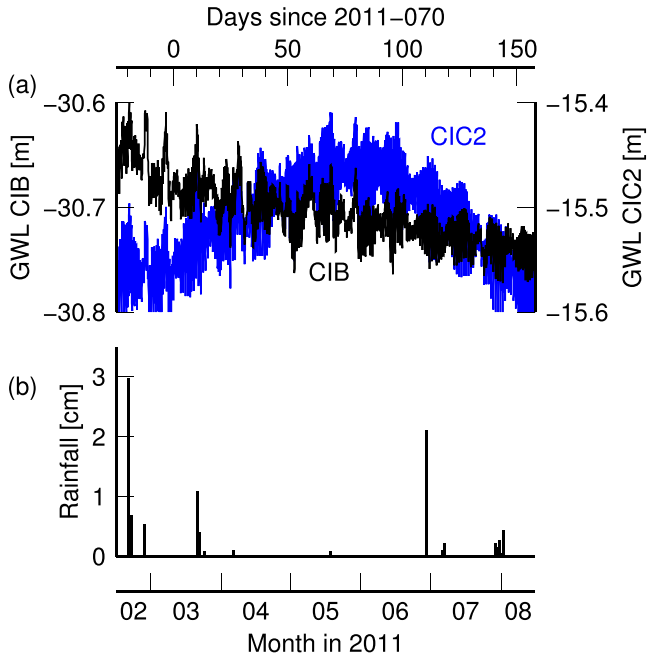

Figure 8. (a) Measurements of the groundwater level (GWL) at the two boreholes indicated in Figure 1. (b) Precipitation at PFO.

4.3. Groundwater Table

A possible mechanism controlling the inverse strain dependence is associated with fluctuations of the groundwater table in response to tidal deformation [*Elkhoury et al.*, 2006]. Clapping under drained conditions controls groundwater levels (GWLs) in fluid-saturated areas. Tidal compression and extension of the pore space lead to a systematic rise and fall of the GWL, where the wetting of shallower porous rocks during compression periods leads to overall reduced seismic wave speeds [*Grêt et al.*, 2006; *Sens-Schönfelder and Wegler*, 2006; *Meier et al.*, 2010; *Hillers et al.*, 2014]. We consider this mechanism and examine water table records (Figure 8a) from two boreholes located in the vicinity of the seismic array (Figure 1). Oscillations of the GWL in both wells are remarkably synchronous with the tidal deformation, i.e., the level rises during compression and falls during extension with an amplitude between 1 and 10 cm. *Sens-Schönfelder and Wegler* [2006] model a ∼0.1% velocity change with GWL fluctuations of the order of 10 m. Our observed 0.03% are thus at the upper limit of the range that can be extrapolated from the amplitude of the oscillations. It should be noted that such estimates depend on assumptions about the length scale of seismic energy diffusion that are usually not well constrained and on the magnitude of the velocity change between drained and undrained conditions.

These observations show that our measured dv/v variations can be driven by systematic GWL changes. To test this hypothesis, we first apply the threshold method to GWL records instead of θ time series. This is expected to yield cleaner results if seismic velocities are governed by the GWL instead of tidal deformation. Second, we consider potentially delayed dv/v changes associated with porosity-controlled equilibration of the water table [*Elkhoury et al.*, 2006]. We apply the threshold method to θ time series that are systematically phase shifted or delayed by 20°–100° and 60–300 min to the original, respectively. In both cases, however, the overall noisier responses do not provide evidence in support of the hypothesis.

Well-level data provide also evidence for the converse insensitivity of seismic wave speeds to GWL fluctuations. Considering that the two wells are only ∼300 m apart, the highly dissimilar, intermittently opposite, trend in the GWL data indicate a complex spatiotemporal hydraulic situation. It varies over spatial scales that are smaller compared to the surface projection of the volume or area sampled by scattered waves in 5–10 s. The GWL records have persistent trends that are likely related to groundwater depletion, superposed with seasonal variations, but they are unlikely governed by the local precipitation pattern (Figure 8b). Importantly, the long-term dv/v trend (Figure 4c) estimated from ZZ correlations is not correlated with any of the two long-term GWL trends. This observation is indicative considering the clear relationship between precipitation-driven GWL models and seismic velocity variations [*Sens-Schönfelder and Wegler*, 2006; *Hillers et al.*, 2014]. Finally, GWL-driven seismic wave speed variations are consistent on all components of the empirical Green's function tensor [*Hillers et al.*, 2014]. Hence, the three different directional responses ZZ, NN, and EE provide the most compelling evidence against a governing role of the GWL at PFO. In summary, a contribution of GWL fluctuations induced by tidal deformation to velocity variations cannot be ruled out, but the compiled observations imply that this contribution is small and does not govern the significant features of the response characteristics.

©2014. American Geophysical Union. All Rights Reserved.

This statement is similar to the above assessment on the role of temperature (section 4.1). Considering likely interactions of simultaneously acting driving mechanisms, some of the remaining ambiguities can be associated with the design of our experiment, i.e., averaging over time segments defined by some deformation, time of day, or GWL threshold. Ideally, velocity variations are monitored in intervals of hours [*Yamamura et al.*, 2003] to extract spectral components and to resolve competing effects on the seismic velocity structure. For seismological applications, however, this requires higher sampling rates and noise power at higher frequencies for correlations to converge at shorter time scales.

4.4. Acoustoelastic Testing and Dilatancy

Extending resonant bar experiments [e.g., *Zinszner et al.*, 1997; *TenCate et al.*, 2004; *Pasqualini et al.*, 2007], modern laboratory "dynamic acoustoelastic testing" experiments study the rheology of dynamically deformed rock samples [*Renaud et al.*, 2011, 2012]. Elasticity of the vibrating samples is monitored by continuously measuring the travel time of high-frequency pulses that propagate perpendicular to the applied direction of strain. *Renaud et al.* [2012] tested the responses of 11 different rock types (dry experiments) and observed for all but the Fontainebleau sandstone sample the expected behavior of wave speed increase during compression. The response is expected because as pores close under increasing confining stress below the elastic limit, the material behaves progressively as an intact solid.

The opposite Fontainebleau behavior is compatible with its extreme response observed in earlier resonant bar experiments [*Zinszner et al.*, 1997; *Pasqualini et al.*, 2007]. The material is characterized by the lowest *P* wave velocity in the sample collection of *Renaud et al.* [2012], indicating a relatively porous, compliant rock with reduced modulus. These are typical characteristics of dilatant materials. Dilatancy is a result of the inelastic irreversible damage induced by microcracking and the associated increase in porosity in samples loaded above the yield stress [e.g., *Brace et al.*, 1966; *Cook*, 1970; *Hadley*, 1976; *Holcomb*, 1981]. More generally, dilatancy is a signature of highly damaged and granular materials under compression [*Ben-Zion*, 2008]. Significantly, seismic wave speeds are reduced during dilatant episodes due to the increase in void space, compatible with our observed ZZ velocity dependence on θ. The increased porosity at the microscopic scale of the Fontainebleau samples is comparable to the macroscopic properties of the weathered, yet not completely decomposed, jointed layer above the granitic basement at PFO. These similarities imply a characteristic signature of porous, incompetent rock types in response to cyclic deformation that is different to the response of more compact, solidified material, and that is consistent across the range of laboratory and the in situ dimensions and strains discussed here.

The importance of dilatant effects is further implied by the observation that deformation associated with waves from regional earthquakes increased the permeability around PFO [*Elkhoury et al.*, 2006]. This leads to reduced phase delays between volumetric tidal compression (extension) and the rising (falling) of the GWL in the two wells. We interpret the shaking-induced increase of the effective pore space as a dilatancy marker that is consistent with the inelastic extension that potentially governs the vertical response associated with the ZZ wave speed changes. GWL rising in response to volumetric compaction is compatible with this situation recognizing that the compacting horizontal strains dominate the fluid response. Together, these results are compatible with the conjecture that dilatant effects contribute to the observed wave speed reductions measured with the vertical component of motion in response to volumetric or horizontal compression.

We recognize a range of similarities between the experimental acoustoelastic testing designs and implications and the method and results discussed in this article. Here tides constitute the continuous source of deformation, and noise correlation coda measurements are equivalent with active source techniques for monitoring the induced travel time changes. We may thus term our approach "passive in situ acoustoelastic testing."

4.5. Component Sensitivity

The analogy of the experimental Fontainebleau results applies to the ZZ S_θ sensitivity but not to the corresponding NN and EE small τ results. However, the conundrum of negative ZZ S_θ disappears if we focus on the parallel sensitivity. By this we mean the sensitivity to the component of deformation that is parallel to the component of wave motion (section 3.2). At early lapse times, velocity changes estimated from ZZ, NN, and EE correlations are consistently positive in response to ε_{UD}, ε_{NS}, and ε_{EW}, respectively. Recall that the reversed polarity of the vertical strain is associated with the Poisson effect, i.e., the material extends in the direction normal to the plane defined by the two maximum stress orientations. Dilatant effects as discussed

©2014. American Geophysical Union. All Rights Reserved.

in the previous section are therefore compatible with this mechanism, although the application of the Poisson effect does not necessarily signify inelastic dilatancy associated with the porosity or damage state of a sample.

The component dependence can be amplified by the sensitivity to different wavefield constituents. Again, the early coda of ZZ correlations is dominated by Rayleigh waves [*Margerin et al.*, 2009], which are polarized in a perpendicular plane to the Love wave motion that is primarily captured in the NN and EE correlations. To verify this notion, we calculate three-component seismograms [*Cotton and Coutant*, 1997] in response to vertical and horizontal forces applied at the surface using the PFO velocity model of *Fletcher et al.* [1990]. The synthetics show that vertical (horizontal) motion is dominated by Rayleigh (Love) waves. This supports the concept that variable wave types with different sensitivities to the anisotropic response of the unconsolidated upper layer contribute to the component dependence of S_θ at small τ.

Directional sensitivities do not, however, readily explain the complex behavior observed on the horizontal components, notably the oscillation in the NN response. However, the low pass or average responses observed on the horizontal correlation components agree, and differences at early lapse times should not distract from the overall similarity of S_θ—in sign and amplitude—on all three components of correlations later in the coda. This similarity is controlled by wave conversions that homogenize the sensitivity of the multiple-scattered coda wavefield on all components.

Different NN and EE results can be an indicator of a horizontally anisotropic strain response. The results motivate more detailed investigations of directional wave speed changes and potentially azimuthal strain sensitivities in response to inhomogeneous deformation patterns. These suggested further investigations address an essential aspect toward a more complete understanding of the observed behavior. That is, our approach of studying the parallel sensitivity does not resolve a potentially more fundamental directional response, which may be better described in an axis system that is rotated with respect to the N-E-Z coordinates.

The general $S_\theta(\tau)$ behavior is well resolved considering the uncertainties. But the scatter around the mean trend in the $d\theta$–dv/v plane indicated by the RMS error (Figures 7b and 7c) at small τ is significantly larger for the horizontal components compared to the ZZ measurements. This can be attributed to hysteretic behavior. However, average NN and EE coda amplitudes tend to be reduced at small τ relative to the ZZ estimates (Figure 2f). Whether this feature is indicative of a systematic material behavior or governed by the generally lower quality of correlations on horizontal components will not be resolved here.

5. Conclusions

In this article we demonstrate the possibility to resolve relative velocity changes ($O(10^{-4})$) in response to tidal strains ($O(10^{-8})$) using ambient noise-based analysis techniques. Processing data collected by a dense temporal array at the Piñon Flat Observatory (PFO), we examine the resolution of two analysis methods. We find that the computationally cheaper threshold method is best applied to test a range of responses in a large parameter space, but the more expensive segment method yields better constraint results for more detailed response estimates.

The key result of our investigation is the component and lapse time dependent sensitivity of relative velocity changes to tidal deformation. The results indicate greater sensitivity near the surface and therefore imply that the response is governed by the rheology of the weathered near-surface layer at PFO overlying the competent granitic basement. Different behavior resolved with the vertical and horizontal correlation components indicates a complex anisotropic in situ rheology. In particular, the negative sensitivity to volumetric deformation resolved with ZZ coda waves at early lapse times—wave speeds are decreased during periods of areal and volumetric compression—contradicts previous observations of near-surface in situ responses to Earth tides. These observations are governed by different wave types constituting the early coda of vertical and horizontal correlation components, which have thus different sensitivities to the anisotropic and possibly (but not necessarily) dilatant behavior.

To the first approximation, the observed response of the material at PFO is in the nonlinear regime [*Agnew*, 1981]. Nonlinearity is inferred from the velocity change induced by tidal strains, since the behavior of a perfectly linear elastic body described by the same modulus during loading and unloading implies constant wave speeds. The in situ nonlinearity across the differential strain range of $\sim 6 \times 10^{-8}$ is consistent with

©2014. American Geophysical Union. All Rights Reserved.

the response induced by similar strains in the laboratory [*TenCate et al.*, 2004; *Pasqualini et al.*, 2007]. Thus, our results extend the compatibility between field and laboratory observations at large strain amplitudes [*Lawrence et al.*, 2008; *Renaud et al.*, 2014] toward a smaller deformation regime.

Conclusions on elasticity are more ambiguous. Inelastic properties are implied by dilatant effects which are suggested by the negative velocity dependence on areal and volumetric deformation observed with the vertical component of wave motion. The decrease in wave speeds is a rheologic property of compliant, damaged rocks under compression or shear load and is therefore compatible with the characteristics of the near-surface layer at the observation site. However, equivalent polarity of the ZZ velocity changes and the deformation in the vertical direction (ε_{UD}) is controlled by the Poisson effect. That is, the medium bulges elastically out of the plane defined by the direction of two maximum compressive stresses, i.e., the horizontal plane. Therefore, inelastic dilatancy is not necessarily required to explain the negative ZZ wave speed changes in response to volumetric deformation. The situation may similarly be governed by a nonlinear (because of $dv/v \neq 0$) elastic Poisson effect. We also do not observe further manifestations of inelastic behavior. A marker of inelasticity is hysteresis during loading-unloading loops [*Holcomb*, 1981; *Agnew*, 1981; *Ostrovsky and Johnson*, 2001], which is due to energy dissipation associated with the irreversible increase in crack density or damage. Reports on the modulation of ambient wavefield properties governed by tidal-induced dissipation changes [*Zaitsev et al.*, 2008] suggest an observable effect of the phenomenon using passive techniques. However, the uncertainty of individual dv/v estimates at a given differential strain does not allow at present the tracking of hysteresis loops. Measures targeting an increase of the resolution [*Stehly et al.*, 2011] can facilitate estimates of dissipation associated with the area between loading and unloading trajectories.

To conclude, we consider it certain that dominant features of the observed sensitivities at early lapse times are collectively governed by the properties of the unconsolidated material in the top tens of meters at the PFO site. The effects are amplified by the directional sensitivities of the different wave types constituting the early coda of vertical and horizontal correlation components. The material response is clearly nonlinear, but definite discrimination between elastic or inelastic behavior in response to tidal forcing needs to await further evidence.

Assuming a bulk modulus of 10^4 MPa, our $S_\theta \approx 5 \times 10^3$ translates into a relative velocity stress sensitivity of 0.5 MPa^{-1}. This is between the 5×10^{-3} MPa^{-1} and 2 MPa^{-1} observed previously in response to tidal loading [*Yamamura et al.*, 2003]. The strain sensitivity is furthermore comparable to the $\sim 10^3$ observed at midcrustal depths in response to a slow-slip event on a subducting interface [*Rivet et al.*, 2011].

The passive in situ acoustoelastic testing method introduced here facilitates a systematic analysis of near-surface responses to tidal deformation. An important advantage compared to earlier tidal monitoring techniques is the independence on a repetitive active source. Long-term passive campaigns are conceivable to monitor systematic variations in the tidal response to tectonic loading [*Yamamura et al.*, 2003] and to study the dependence on variable rock properties and effective and confining stresses [*Zinszner et al.*, 1997; *Stanchits et al.*, 2006]. More generally, the approach has the potential to become a building block of observational tools to investigate velocity response types of crustal and fault zone materials to continuous, periodic, and transient deformation of variable duration and amplitude. Responses to the generally well modeled timing and amplitude of the tidal deformation history can help to calibrate dv/v responses to other perturbations, e.g., transients associated with earthquake fault slip, environmental changes exhibiting seasonal patterns, and volcanic fluid migration. Where noise-based techniques have been applied to monitor relative velocity changes in response to these mechanisms, the reported dv/v amplitudes are collectively larger than the 0.03% reported here, which has two implications. First, averaging over time scales comparable to the dominant frequency of the deformation likely destroys the tidal signal, as suggested by our time-averaging analysis. This encourages further research targeting the decomposition of dv/v time series for the isolation or suppression of signals associated with different interfering loading mechanisms [*Furumoto et al.*, 2001; *Hobiger et al.*, 2012; *Richter et al.*, 2014; *Brenguier et al.*, 2014]. Second, differences in loading period (e.g., seasonal versus tidal) may lead to frequency-dependent dv/v amplitudes, a dispersive behavior that is well known from laboratory experiments [*Holcomb*, 1981; *Jaeger et al.*, 2007].

Much of our knowledge concerning the rheology of rocks rests on results obtained from perturbations of samples under controlled laboratory conditions. Results of the approach presented here indicate that

©2014. American Geophysical Union. All Rights Reserved.

seismologists can further contribute to the discussion by providing high-resolution observations of in situ behavior. Future studies from different tectonic environments targeting materials characterized by variable degrees of damage may thus extend, support, or modify interpretations based on laboratory experiments.

Acknowledgments

We thank D. Agnew for providing us with the predicted tidal strain, and the water well and meteorological data, from PFO. We appreciate discussions with P.A. Johnson, M.L. Doan, E. Daub, and G. Renaud. This work was supported by the European Research Council (Advanced grant Whisper L27507). G. Hillers acknowledges support through a Heisenberg fellowship from the German Research Foundation (Hi 1714/1-1). Figures were made using Generic Mapping Tools (GMT) [*Wessel and Smith*, 1998] with global multiresolution topography (GMRT) [*Ryan et al.*, 2009]. We thank X. Briand for his outstanding and timely computational assistance that underpinned much of this work and O. Coutant for providing the waveform synthetics. We thank the Associate Editor, N. Nakata, and an anonymous reviewer for their comments that helped to improve the manuscript. The field experiment was funded by USGS grant G11AP20056. Retrieval of the original seismograms from the IRIS Data Management Center is sufficient to understand, evaluate, replicate, and build upon the reported research.

References

Agnew, D. C. (1981), Nonlinearity in rock: Evidence from Earth tides, *J. Geophys. Res.*, *86*(B5), 3969–3978.

Agnew, D. C., and F. K. Wyatt (2014), Long-term high-quality deformation observations with long-base strainmeters, *Annual SCEC Meeting Poster 218*, Palm Springs, Calif.

Allam, A. A., and Y. Ben-Zion (2012), Seismic velocity structures in the Southern California plate-boundary environment from double-difference tomography, *Geophys. J. Int.*, *190*, 1181–1196, doi:10.1111/j.1365-246X.2012.05544.x.

Anache-Ménier, D., B. A. van Tiggelen, and L. Margerin (2009), Phase statistics of seismic coda waves, *Phys. Rev. Lett.*, *102*(24), 248501, doi:10.1103/PhysRevLett.102.248501.

Ben-Zion, Y. (2008), Collective behavior of earthquakes and faults: Continuum-discrete transitions, progressive evolutionary changes and different dynamic regimes, *Rev. Geophys.*, *46*, RG4006, doi:10.1029/2008RG000260.

Brace, W. F., B. W. Paulding, and C. Scholz (1966), Dilatancy in the fracture of crystalline rocks, *J. Geophys. Res.*, *71*(16), 3939–3953.

Brenguier, F., N. M. Shapiro, M. Campillo, V. Ferrazzini, Z. Duputel, O. Coutant, and A. Nercessian (2008), Towards forecasting volcanic eruptions using seismic noise, *Nat. Geosci.*, *1*, 126–130, doi:10.1038/ngeo104.

Brenguier, F., M. Campillo, T. Takeda, Y. Aoki, N. M. Shapiro, X. Briand, K. Emoto, and H. Miyake (2014), Mapping pressurized volcanic fluids from induced crustal seismic velocity drops, *Science*, *345*(6192), 80–82, doi:10.1126/science.1254073.

Bungum, H., T. Risbo, and E. Hjortenberg (1977), Precise continuous monitoring of seismic velocity variations and their possible connection to solid Earth tides, *J. Geophys. Res.*, *82*(33), 5365–5373.

Campillo, M., H. Sato, N. M. Shapiro, and R. D. van der Hilst (2011), New developments on imaging and monitoring with seismic noise, *C. R. Geosci.*, *343*, 487–495, doi:10.1016/j.crte.2011.07.007.

Clarke, D., L. Zaccarelli, N. M. Shapiro, and F. Brenguier (2011), Assessment of resolution and accuracy of the Moving Window Cross Spectral technique for monitoring crustal temporal variations using ambient seismic noise, *Geophys. J. Int.*, *186*, 867–882, doi:10.1111/j.1365-246X.2011.05074.x.

Cook, N. G. W. (1970), An experiment proving that dilatancy is a pervasive volumetric property of brittle rock loaded to failure, *Rock Mech.*, *2*, 181–188.

Cotton, F., and O. Coutant (1997), Dynamic stress variations due to shear faults in a plane-layered medium, *Geophys. J. Int.*, *128*, 676–688.

Custodio, S. I. S., J. F. B. D. Fonseca, N. F. d'Oreye, B. V. E. Faria, and Z. Bandomo (2003), Tidal modulation of seismic noise and volcanic tremor, *Geophys. Res. Lett.*, *30*(15), 1816, doi:10.1029/2003GL016991.

DeWolf, S. (2014), Optical fiber sensors for infrasonic wind noise reduction and Earth strain measurement, PhD thesis, Univ. of California, San Diego, Calif.

Elkhoury, J. E., E. E. Brodsky, and D. C. Agnew (2006), Seismic waves increase permeability, *Nature*, *441*(29), 1135–1138, doi:10.1038/nature04798.

Fletcher, J. B., T. Fumal, H.-P. Liu, and L. C. Carroll (1990), Near-surface velocities and attenuation at two boreholes near Anza, California, from logging data, *Bull. Seismol. Soc. Am.*, *80*(4), 807–831.

Furumoto, M., Y. Ichimori, N. Hayashi, and Y. Hiramatsu (2001), Seismic wave velocity changes and stress build-up in the crust of the Kanto-Tokai region, *Geophys. Res. Lett.*, *28*(19), 3737–3740.

Gao, S. G., P. G. Silver, A. T. Linde, and I. S. Sacks (2000), Annual modulation of triggered seismicity following the 1992 Landers earthquake in California, *Nature*, *406*, 500–504.

Grêt, A., R. Snieder, and J. Scales (2006), Time-lapse monitoring of rock properties with coda wave interferometry, *J. Geophys. Res.*, *111*, B03305, doi:10.1029/2004JB003354.

Hadley, K. (1976), Comparison of calculated and observed crack densities and seismic velocities in Westerly granite, *J. Geophys. Res.*, *81*(20), 3484–3494.

Hadziioannou, C., E. Larose, O. Coutant, P. Roux, and M. Campillo (2009), Stability of monitoring weak changes in multiply scattering media with ambient noise correlations: Laboratory experiments, *J. Acoust. Soc. Am.*, *125*(6), 3688–3695, doi:10.1121/1.3125345.

Hamiel, Y., O. Katz, V. Lyakhovsky, Z. Reches, and Y. Fialko (2006), Stable and unstable damage evolution in rocks with implications to fracturing of granite, *Geophys. J. Int.*, *167*, 1005–1016, doi:10.1111/j.1365-246X.2006.03126.x.

Herrmann, R. B. (2006), Computer programs in seismology, vers. 3.30: An overview of synthetic seismogram computation, *Tech. Rep.*, Saint Louis Univ., Mo.

Hillers, G., and Y. Ben-Zion (2011), Seasonal variations of observed noise amplitudes at 2–18 Hz in southern California, *Geophys. J. Int.*, *184*, 860–868, doi:10.1111/j.1365-246X.2010.04886.x.

Hillers, G., M. Campillo, Y.-Y. Lin, K.-F. Ma, and P. Roux (2012), Anatomy of the high-frequency ambient seismic wave field at the TCDP borehole, *J. Geophys. Res.*, *117*, B06301, doi:10.1029/2011JB008999.

Hillers, G., M. Campillo, and K.-F. Ma (2014), Seismic velocity variations at TCDP are controlled by MJO driven precipitation pattern and high fluid discharge properties, *Earth Planet. Sci. Lett.*, *391*, 121–127, doi:10.1016/j.epsl.2014.01.040.

Hobiger, M., U. Wegler, K. Shiomi, and H. Nakahara (2012), Coseismic and postseismic elastic wave variations caused by the 2008 Iwate-Miyagi Nairiku earthquake, Japan, *J. Geophys. Res.*, *117*, B09313, doi:10.1029/2012JB009402.

Holcomb, D. J. (1981), Memory, relaxation, and microfracturing in dilatant rock, *J. Geophys. Res.*, *86*(B7), 6235–6248.

Hong, T.-K., and W. Menke (2006), Tomographic investigation of the wear along the San Jacinto fault, southern California, *Phys. Earth Planet. Inter.*, *155*, 236–248.

Jaeger, J. C., N. G. W. Cook, and R. W. Zimmermann (Eds.) (2007), *Fundamentals of Rock Mechanics*, 475 pp., 4th ed., Blackwell, Oxford, U. K.

Johnson, P. A., H. Savage, M. Knuth, J. Gomberg, and C. Marone (2008), Effects of acoustic waves on stick-slip in granular media and implications for earthquakes, *Nature*, *451*, 57–60, doi:10.1038/nature06440.

Larose, E., A. Khan, Y. Nakamura, and M. Campillo (2005), Lunar subsurface investigated from correlation of seismic noise, *Geophys. Res. Lett.*, *33*, L16201, doi:10.1029/2005GL023518.

Larose, E., P. Roux, and M. Campillo (2007), Reconstruction of Rayleigh-Lamb dispersion spectrum based on noise obtained from an air-jet forcing, *J. Acoust. Soc. Am.*, *122*(6), 3437–3444, doi:10.1121/1.2799913.

©2014. American Geophysical Union. All Rights Reserved.

Lawrence, Z., P. Bodin, C. A. Langston, F. Pearce, J. Gomberg, P. A. Johnson, F.-Y. Menq, and T. Brackman (2008), Induced dynamic nonlinear ground responses at Garner Valley, California, *Bull. Seismol. Soc. Am.*, *98*(3), 1412–1428, doi:10.1785/0120070124.

Lobkis, O. I., and R. L. Weaver (2003), Coda-wave interferometry in finite solids: Recovery of *P*-to-*S* conversion rates in an elastodynamic billiard, *Phys. Rev. Lett.*, *90*(25), 254302, doi:10.1103/PhysRevLett.90.254302.

Lockner, D. A., J. B. Walsh, and J. D. Byerlee (1977), Changes in seismic velocity and attenuation during deformation of granite, *J. Geophys. Res.*, *82*(33), 5374–5378.

Lyakhovsky, V., Z. Reches, R. Weinberger, and T. E. Scott (1997), Non-linear elastic behavior of damaged rocks, *Geophys. J. Int.*, *130*, 157–166.

Margerin, L., M. Campillo, B. A. van Tiggelen, and R. Hennino (2009), Energy partition of seismic coda waves in layered media: Theory and application to Pinyon Flats Observatory, *Geophys. J. Int.*, *177*, 571–585, doi:10.1111/j.1365-246X.2008.04068.x.

Meier, U., N. M. Shapiro, and F. Brenguier (2010), Detecting seasonal variations in seismic velocities within Los Angeles basin from correlations of ambient seismic noise, *Geophys. J. Int.*, *181*, 985–996, doi:10.1111/j.1365-246X.2010.04550.x.

Nakata, R., N. Suda, and H. Tsuruoka (2008), Non-volcanic tremor resulting from the combined effect of Earth tides and slow slip events, *Nat. Geosci.*, *1*, 676–678, doi:10.1038/ngeo28ci.

Niu, F., P. G. Silver, T. M. Daley, X. Cheng, and E. L. Majer (2008), Preseismic velocity changes observed from active source monitoring at the Parkfield SAFOD drill site, *Nature*, *454*, 204–208, doi:10.1038/nature07111.

Obermann, A., T. Planès, E. Larose, C. Sens-Schönfelder, and M. Campillo (2013), Depth sensitivity of seismic coda waves to velocity perturbations in an elastic heterogeneous medium, *Geophys. J. Int.*, *194*(1), 372–382, doi:10.1093/gji/ggt043.

Ostrovsky, L. A., and P. A. Johnson (2001), Dynamic nonlinear elasticity in geomaterials, *Riv. Nuovo Cimento*, *24*(7), 1–46.

Pasqualini, D., K. Heitmann, J. A. TenCate, S. Habib, D. Higdon, and P. A. Johnson (2007), Nonequilibrium and nonlinear dynamics in Berea and Fontainebleau sandstones: Low-strain regime, *J. Geophys. Res.*, *112*, B01204, doi:10.1029/2006JB004264.

Poli, P., H. A. Pedersen, M. Campillo, and the POLENET/LAPNET Working Group (2012), Emergence of body waves from cross-correlation of short period seismic noise, *Geophys. J. Int.*, *188*, 549–558, doi:10.1111/j.1365-246X.2011.05271.x.

Poupinet, G., W. Ellsworth, and J. Frechet (1984), Monitoring velocity variations in the crust using earthquake doublets: An application to the Calaveras Fault, California, *J. Geophys. Res.*, *89*(B7), 5719–5731.

Reasenberg, P., and K. Aki (1974), A precise, continuous measurement of seismic velocity for monitoring in situ stress, *J. Geophys. Res.*, *79*(2), 399–406.

Renaud, G., M. Talmant, S. Callé, M. Defontaine, and P. Laugier (2011), Nonlinear elastodynamics in micro-inhomogeneous solids observed by head-wave based dynamic acoustoelastic testing, *J. Acoust. Soc. Am.*, *130*(6), 3583–3589, doi:10.1121/1.3652871.

Renaud, G., P.-Y. L. Bas, and P. A. Johnson (2012), Revealing highly complex elastic nonlinear (anelastic) behavior of Earth materials applying a new probe: Dynamic acoustoelastic testing, *J. Geophys. Res.*, *117*, B06202, doi:10.1029/2011JB009127.

Renaud, G., J. Rivière, C. Larmat, J. T. Rutledge, R. C. Lee, R. A. Guyer, K. Stokoe, and P. A. Johnson (2014), In situ characterization of shallow elastic nonlinear parameters with Dynamic Acoustoelastic Testing, *J. Geophys. Res. Solid Earth*, *119*, 6907–6923, doi:10.1002/2013JB010625.

Richter, T., C. Sens-Schönfelder, R. Kind, and G. Asch (2014), Comprehensive observation and modeling of earthquake and temperature-related seismic velocity changes in northern Chile with passive image interferometry, *J. Geophys. Res. Solid Earth*, *119*, 4747–4765, doi:10.1002/2013JB010695.

Rivet, D., M. Campillo, N. M. Shapiro, V. Cruz-Atienza, M. Radiguet, N. Cotte, and V. Kostoglodov (2011), Seismic evidence of nonlinear crustal deformation during a large slow slip event in Mexico, *Geophys. Res. Lett.*, *38*, L08308, doi:10.1029/2011GL047151.

Rubinstein, J. L., M. L. Rocca, J. E. Vidale, K. C. Creager, and A. G. Wech (2008), Tidal modulation of nonvolcanic tremor, *Science*, *319*, 186–189, doi:10.1126/science.1150558.

Ryan, W. B. F., et al. (2009), Global multi-resolution topography synthesis, *Geochem. Geophys. Geosyst.*, *10*, Q03014, doi:10.1029/2008GC002332.

Sabra, K. G., P. Gerstoft, P. Roux, W. A. Kuperman, and M. C. Fehler (2005), Surface wave tomography from microseisms in Southern California, *Geophys. Res. Lett.*, *32*, L14311, doi:10.1029/2005GL023155.

Schaff, D. P. (2012), Placing an upper bound on preseismic velocity changes measured by ambient noise monitoring for the 2004 M_W 6.0 Parkfield Earthquake (California), *Bull. Seismol. Soc. Am.*, *102*(4), 1400–1416, doi:10.1785/0120110342.

Scholz, C. H. (Ed.) (2002), *The Mechanics of Earthquakes and Faulting,* 2nd ed., 471 pp., Cambridge Univ. Press, Cambridge, U. K.

Sens-Schönfelder, C., and U. Wegler (2006), Passive image interferometry and seasonal variations of seismic velocities at Merapi Volcano, Indonesia, *Geophys. Res. Lett.*, *33*, L21302, doi:10.1029/2006GL027797.

Silver, P. G., T. M. Daley, F. Niu, and E. L. Majer (2007), Active source monitoring of cross-well seismic travel time for stress-induced changes, *Bull. Seismol. Soc. Am.*, *97*(1B), 281–293, doi:10.1785/0120060120.

Stanchits, S., S. Vinciguerra, and G. Dresen (2006), Ultrasonic velocities, acoustic emission characteristics and crack damage of basalt and granite, *Pure Appl. Geophys.*, *163*, 974–993, doi:10.1007/s00024-006-0059-5.

Stehly, L., M. Campillo, B. Froment, and R. L. Weaver (2008), Reconstructing Green's function by correlation of the coda of the correlation (C^3) of ambient seismic noise, *J. Geophys. Res.*, *113*, B11306, doi:10.1029/2008JB005693.

Stehly, L., P. Cupillard, and B. Romanowicz (2011), Towards improving ambient noise tomography using simultaneously curvelet denoising filters and SEM simulations of seismic ambient noise, *C. R. Geosci.*, *343*, 591–599, doi:10.1016/j.crte.2011.03.005.

Stroup, D. F., D. R. Bohnenstiehl, M. Tolstoy, F. Waldhauser, and R. T. Weekly (2007), Pulse of the seafloor: Tidal triggering of microearthquakes at 9°50′N East Pacific Rise, *Geophys. Res. Lett.*, *34*, L15301, doi:10.1029/2007GL030088.

Takano, T., T. Nishimura, H. Nakahara, Y. Ohta, and S. Tanaka (2014), Seismic velocity changes caused by the Earth tide: Ambient noise correlation analyses of small-array data, *Geophys. Res. Lett.*, *41*, 6131–6136, doi:10.1002/2014GL060690.

TenCate, J. A., D. Pasqualini, S. Habib, K. Heitmann, D. Higdon, and P. A. Johnson (2004), Nonlinear and nonequilibrium dynamics in geomaterials, *Phys. Rev. Lett.*, *93*(6), 065501, doi:10.1103/PhysRevLett.93.065501.

Tsuruoka, H., M. Ohtake, and H. Sato (1995), Statistical test of the tidal triggering of earthquakes: Contribution of the ocean tide loading effect, *Geophys. J. Int.*, *122*, 183–194.

Vernon, F. L., J. Fletcher, L. Carroll, A. Chave, and E. Sembera (1991), Coherence of seismic body waves from local events as measured by a small-aperture array, *J. Geophys. Res.*, *96*(B7), 11,981–11,996.

Vernon, F. L., G. L. Pavlis, T. J. Owens, D. E. McNamara, and P. N. Anderson (1998), Near-surface scattering effects observed with a high-frequency phased array at Pineon Flats, California, *Bull. Seismol. Soc. Am.*, *88*(6), 1548–1560.

Wagner, G. S. (1998), Local wave propagation near the San Jacinto Fault Zone, southern California: Observations from a three-component seismic array, *J. Geophys. Res.*, *103*(B4), 7231–7246.

©2014. American Geophysical Union. All Rights Reserved.

Weaver, R. L., B. Froment, and M. Campillo (2009), On the correlation of non-isotropically distributed ballistic scalar diffuse waves, *J. Acoust. Soc. Am.*, *126*(4), 1817–1826, doi:10.1121/1.3203359.

Weaver, R. L., C. Hadziioannou, E. Larose, and M. Campillo (2011), On the precision of noise correlation interferometry, *Geophys. J. Int.*, *185*, 1384–1392, doi:10.1111/j.1365-246X.2011.05015.x.

Wegler, U., and C. Sens-Schönfelder (2007), Fault zone monitoring with passive image interferometry, *Geophys. J. Int.*, *168*, 1029–1033, doi:10.1111/j.1365-246X.2006.03284.

Wessel, P., and W. H. F. Smith (1998), New, improved version of generic mapping tools released, *Eos Trans. AGU*, *79*(47), 579–579, doi:10.1029/98EO00426.

Wyatt, F. (1982), Displacement of surface monuments: Horizontal motion, *J. Geophys. Res.*, *87*(B2), 979–989.

Yamamura, K., O. Sano, H. Utada, Y. Takei, S. Nakao, and Y. Fukao (2003), Long-term observation of in situ seismic velocity and attenuation, *J. Geophys. Res.*, *108*(B6), 2317, doi:10.1029/2002JB002005.

Zaccarelli, L., N. M. Shapiro, L. Faenza, G. Soldati, and A. Michelini (2011), Variations of crustal elastic properties during the 2009 L'Aquila earthquake inferred from cross-correlations of ambient seismic noise, *Geophys. Res. Lett.*, *38*, L24304, doi:10.1029/2011GL049750.

Zaitsev, V. Y., V. A. Saltykov, and L. A. Matveev (2008), Relation between the tidal modulation of seismic noise and the amplitude-dependent loss in rock, *Acoust. Phys.*, *54*(4), 538–544.

Zhan, Z., V. C. Tsai, and R. W. Clayton (2013), Spurious velocity changes caused by temporal variations in ambient noise frequency content, *Geophys. J. Int.*, *194*(3), 1574–1581, doi:10.1093/gji/ggt170.

Zigone, D., Y. Ben-Zion, M. Campillo, and P. Roux (2014), Seismic tomography of the Southern California plate boundary region from noise-based Rayleigh and Love Waves, *Pure Appl. Geophys.*, doi:10.1007/s00024-014-0872-1.

Zinszner, B., P. A. Johnson, and P. N. J. Rasolofosaon (1997), Influence of change in physical state on elastic nonlinear response in rock: Significance of effective pressure and water saturation, *J. Geophys. Res.*, *102*(B4), 8105–8120.

©2014. American Geophysical Union. All Rights Reserved.